ACS APPLIED ELECTRONIC MATERIALS

Open Access



pubs.acs.org/acsaelm

Article

# Stable n-Type Conduction in $WO_x$-CNT Hybrid Films

Ayesha Farooq, Luca Bignardi,* Matus Stredansky, Marco Caputo, Sharath Sasikumar, Ferdinando Bassato, Regina Ciancio, Simone Dal Zilio, Andrea Goldoni, Paolo Piseri, Tommaso Mazza, Silvia Rubini, and Cinzia Cepek*

Cite This: *ACS Appl. Electron. Mater.* 2025, 7, 10438−10445

Read Online

ACCESS | Metrics & More | Article Recommendations | Supporting Information

**ABSTRACT:** Nanostructured hybrid films composed of tungsten oxide ($WO_x$) nanoclusters and vertically aligned carbon nanotubes (CNTs) were synthesized through a combination of chemical vapor deposition and supersonic cluster beam deposition. The use of a cluster source enabled the direct fabrication of oxygen-deficient, nonstoichiometric $WO_x$ nanoclusters, which decorated the CNT sidewalls with a characteristic "beaded necklace-style" morphology. Electrical resistance measurements under ethanol exposure in ultrahigh vacuum revealed a distinct behavior consistent with n-type conduction, unlike the intrinsic p-type behavior of pristine CNTs and of $WO_x$ films. This inversion is linked to the appearance of an interfacial charge transfer from the oxygen vacancies in the defective $WO_x$ nanoclusters to the CNTs, which injects electrons into the CNT network and shifting its Fermi level, thereby inverting the conduction type. Notably, this n-type conduction response remained stable even after prolonged air exposure. These results propose a viable approach to achieving air-stable n-type doping in CNT-based nanostructures.

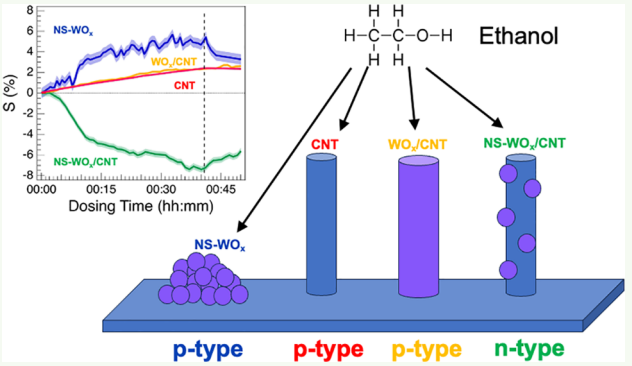


**KEYWORDS:** *tungsten oxide nanoclusters, carbon nanotube hybrids, hybrid nanostructures, supersonic cluster beam deposition, gas sensing, n-type conduction*



## INTRODUCTION

Hybrid materials represent a broad family of systems in which the integration of distinct components enables multifunctional properties that exceed those of the individual constituents.[1,2] Within this context, carbon-based nanomaterials have emerged as a particularly versatile and widely explored platform, often serving as the structural and electronic backbone of advanced hybrid architectures. Among them, carbon nanotubes (CNTs) stand out for their exceptional mechanical strength, high electrical conductivity, and large specific surface area. They also provide robust and flexible scaffolds for hybridization with other nanomaterials, unlocking complementary functionalities such as catalytic activity, light responsiveness, and tunable charge transport.[3−6] Moreover, their quasi-one-dimensional geometry supports ballistic electron transport over micrometer-scale distances, making CNTs highly attractive building blocks for next-generation electronic devices and sensors.[7−11]

Transition metal oxides have also become essential components in the development of functional hybrid systems, owing to their diverse chemical compositions, rich defect chemistry, and highly tunable electronic properties. Among these, tungsten oxides ($WO_x$) stand out for the adaptable stoichiometry and electronic versatility, which can be finely tuned through oxygen vacancy engineering and controlled oxidation states. These characteristics make these oxides ideally suited for a broad range of applications, including gas sensing, photocatalysis, electrochromic devices, and energy storage technologies.[12−20]

Oxygen vacancies and interfacial donor states are recognized as key factors governing electronic behavior in transition-metal oxides. Greiner and co-workers[21] demonstrated that defect-induced modifications in the oxide electronic structure facilitate charge-transfer processes, thereby enhancing n-type conductivity and catalytic activity. In a broader context, Tokura and Nagaosa[22] highlighted that defects in transition-metal oxides can trigger orbital reconstruction and emergent charge-transport phenomena. Reports on $WO_3$ align well with this framework, with several studies showing that oxygen vacancies drive electron-donor behavior, enhance carrier density, and promote interfacial charge transfer.[13,15,23] These outcomes suggest that the defect concentrations can be a viable route to

**Received:** September 12, 2025
**Revised:** November 5, 2025
**Accepted:** November 6, 2025
**Published:** November 17, 2025

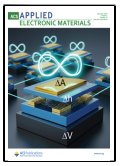

improving electronic transport in composite materials. When combined with CNTs, their intrinsic redox activity and oxygen-vacancy-driven sensing capabilities can be effectively coupled with the exceptional conductivity, high aspect ratio, and mechanical robustness of the carbon backbone. Such a combination enables hybrid systems with tailored interfacial chemistry, enhanced charge-transfer dynamics, and multifunctional behavior that would be difficult to achieve with either component alone.

Hybrid nanostructures that integrate CNTs with inorganic materials therefore offer unique opportunities to exploit synergistic effects and engineer advanced sensing platforms. Numerous studies have demonstrated that composites based on $WO_x$ and CNTs exhibit superior gas-sensing performance compared to their individual constituents, showing higher sensitivity, improved selectivity, and faster response and recovery times.[15,24−34] Although the precise origin of this enhanced performance is not yet fully understood, it is commonly attributed to the formation of p−n heterojunctions at the $WO_x$-CNT interface, which facilitate efficient charge separation and modulate the electrical response of the sensor upon gas adsorption.[25,32,33] Beyond electronic structure, the morphology and nanostructure of the oxide play a critical role: architectures such as nanorods, nanowires, and hierarchical assemblies dramatically increase the surface-to-volume ratio, provide abundant adsorption sites, and accelerate surface reactions.[14,16]

Interfacial effects are particularly significant in these hybrid systems, as interactions between $WO_x$ and CNTs can lead to doping effects that fundamentally alter charge-carrier concentration and band alignment. Depending on the chemical environment and degree of oxide reduction, both p-type and n-type doping can occur, thereby allowing control over sensitivity, response direction, and recovery dynamics. This tunability enables efficient device operation even at room temperature, a major advantage over conventional metal oxide sensors that typically require elevated operating temperatures.[32] Further studies have shown that $WO_x$ clusters themselves can act as electron donors, transferring charge to the underlying CNTs. In particular, reduced $WO_x$ species with a high density of oxygen vacancies are predicted to inject electrons into the CNT network, shifting its Fermi level and potentially inverting the conduction type relative to pristine CNTs.[33,35] Despite these advances, maintaining the stability of such interfacial charge transfer under ambient conditions remains an significant challenge and a central focus of ongoing research.

Various methods have been employed to fabricate $WO_x$-CNT hybrid nanostructures, enabling precise control over oxide morphology and distribution across the carbon nanotube network, which is crucial for tailoring their physical, chemical, and electronic properties. Beyond structural and functional optimization, several studies have emphasized that the interfacial characteristics between $WO_x$ and CNTs are key to achieving reliable and sensitive gas sensing, particularly under ambient conditions.[24,26,31]

In this work, we investigated a novel $WO_x$-CNT nanostructured hybrid prepared by depositing $WO_x$ nanoclusters generated with a supersonic cluster beam deposition (SCBD) source onto vertically aligned CNTs grown by chemical vapor deposition (CVD) on a silicon wafer substrate. SCBD enabled the controlled decoration of the CNTs with $WO_x$ nanoclusters, producing a distinctive "beaded necklace" morphology composed of discrete oxide nanoparticles anchored along the CNT walls—an architecture that, to the best of our knowledge, had not been previously reported. The synthesized hybrids were comprehensively characterized using in situ and ex situ techniques, including X-ray photoelectron spectroscopy (XPS), scanning electron microscopy (SEM), and transmission electron microscopy (TEM). Their chemical and electrical resistive responses to ethanol (EtOH) exposure in UHV were evaluated by monitoring resistance changes. We found that the response toward EtOH was radically different from that observed for pristine CNTs or for a $WO_x$ layer grown on a Si wafer. Remarkably, the hybrids exhibited a behavior which is compatible with n-type conduction upon ethanol exposure, in stark contrast to the p-type response of pristine CNTs or a $WO_x$ film on Si.

## EXPERIMENTAL SECTION

**Material Preparation and Characterization.** Vertically aligned CNTs were synthesized via chemical vapor deposition (CVD) using acetylene as the carbon source and Fe (99.9% purity, 1.5 nm thickness) as the catalyst. The catalyst was deposited by electron-beam evaporation onto alumina films (thickness: 7.5 nm), which were themselves grown by DC magnetron sputtering (DCMS) on Si wafers. Prior to CNT growth, the substrate was degassed at 870 K and subsequently annealed in 100 sccm of $H_2$ (grade 5) for 5 min. Growth was initiated by introducing a gas mixture of $C_2H_2$ (100 sccm, grade 2.5) and $H_2$ (100 sccm, grade 5) at 870 K for 15 s. The growth pressure was maintained at approximately $10^{-4}$ mbar, with a base pressure of $\sim 10^{-6}$ mbar. The length of the resulting CNTs forest was approximately 5 $\mu$m.

Nanostructured $WO_x$ (NS-$WO_x$) clusters were synthesized at the INSPECT Laboratory (IOM-CNR, Trieste) using a supersonic cluster beam deposition (SCBD) source directly connected to the UHV chamber hosting both the photoemission station and the chamber for ethanol exposure.[36] In the SCBD source, a tungsten rod (6mm diameter, 99.9% purity, EvoChem GmbH) was ablated by ion bombardment in an electric discharge ignited after the injection of an inert/$O_2$ gas mixture (0−0.5% $O_2$ in Ar, produced by dosing from two separate gas lines: high-purity Ar 6.0 and 20% $O_2$ in He 6.0). The resulting plasma generated a supersonic beam of neutral $WO_x$ clusters, which were focused by an aerodynamic lens and directed into the ultrahigh-vacuum chamber. The gas composition during deposition was monitored in real time using a residual gas analyzer (SRS RGA200) mounted on the UHV chamber.

DC magnetron sputtering (DCMS) deposition was performed using a tungsten target (99.95% purity) operated at 300 W DC power. Deposition was conducted in an Ar/$O_2$ gas mixture (Ar: 20−23 sccm; $O_2$: 3 sccm), yielding a deposition rate of approximately 0.4 nm $s^{-1}$ at a base pressure of $\sim 10^{-4}$ mbar.

X-ray photoelectron spectroscopy (XPS) measurements were carried out at the INSPECT Laboratory using a Mg K$\alpha$ source ($h\nu$ = 1253.6 eV) and a hemispherical PSP electron analyzer, with an overall energy resolution of approximately 0.8 eV. Spectra were collected in normal emission and referenced to the C 1s peak at 284.4 eV on the binding energy scale.[37] Spectral fitting was performed using Doniach−Šunjić line profiles combined with a Shirley-type background. The Lorentzian width was fixed to literature values,[37] while Gaussian width, intensities, and peak positions were left as free parameters.

SEM images were acquired using ZEISS Supra 40 and LEO XB 1540 SEM-FIB scanning electron microscopes. TEM specimens were prepared by gently scratching the sample surface with a small blade and depositing the collected material onto carbon-coated copper grids. High-resolution TEM (HR/TEM) investigations were performed using a JEOL 2010 UHR field-emission gun microscope equipped with a field-emission Schottky cathode and operated at 200 kV with a spherical aberration coefficient $C_s$ of 0.47 ± 0.01 mm,


https://doi.org/10.1021/acsaelm.5c01933
ACS Appl. Electron. Mater. 2025, 7, 10438−10445

achieving a resolution of 0.19 nm under optimal phase-contrast imaging conditions.

**Ethanol Exposure and Resistive Response Measurements.** A set of measurements of the resistive response upon ethanol exposure was carried out for each sample. These measurements were performed in ultrahigh vacuum (UHV, base pressure: $2 \times 10^{-10}$ mbar) while keeping the sample at room temperature (300 K). Ethanol vapor was introduced into the UHV chamber at a pressure of $2 \times 10^{-5}$ mbar (equivalent to approximately 20 ppb at 1 atm) via a leak valve connected to a dedicated stainless-steel reservoir. Prior to use, ethanol was degassed by several freeze−pump−thaw cycles. The vapor composition during exposure was monitored using a residual gas analyzer. The ethanol reservoir was maintained at approximately 370 K during dosing to achieve the desired vapor pressure in the chamber. Due to the low pumping speed of ethanol, pressure recovery after exposure was slow (approximately 90 min to return to $10^{-7}$ mbar), which limited postexposure recovery measurements.

In the resistive response experiments, two tantalum (Ta) electrodes (approximately $2 \times 2$ mm$^2$ area) were gently brought into contact with the top surface of the investigated film, and the electrical resistance was measured in-plane through the overlayer film under UHV conditions. A schematic of the measuring geometry is reported in the Supporting Information, Figure S1. The contact resistance between the Ta pads and the film was minimized by fine-tuning the electrode pressure and monitoring the stability of the baseline resistance prior to gas exposure. Since the measurements report relative resistance changes rather than absolute conductivity values, any residual contact resistance does not affect the observed response trends. Electrical resistance was recorded using a precision multimeter connected to the tantalum contact pads. Baseline resistances ranged from ohms to megaohms, with less than 1% drift in the absence of ethanol.

The sensitivity ($S$) was defined as

$$S = \frac{\Delta R}{R_0} \times 100 = \frac{R_d - R_0}{R_0} \times 100$$

where $R_0$ is the initial resistance and $R_d$ is the resistance measured during ethanol exposure. Assuming that $\Delta R/R_0$ was proportional to the number of adsorbed molecules, and given that pressure was proportional to dose, the resistance response as a function of dose could be approximated by an adsorption isotherm, as demonstrated in our previous work.[38] Minor nonlinearities in $S$ vs. time arise from small pressure fluctuations due to temperature variations in the EtOH reservoir.

## RESULTS AND DISCUSSION

**Characterization of the Materials.** As described in the Experimental Section, the NS-WO$_x$/CNT hybrids were prepared by exposing the previously synthesized CNTs forest on Si wafers to a beam of WO$_x$ clusters generated by the SCBD source. The morphology of the initial CNT carpet ($434 \pm 4$ CNTs/$\mu$m$^2$), as observed by SEM, is shown in Figure 1a.

Figure 1b shows the SEM images acquired on the NS-WO$_x$/CNT hybrids. The nanoclusters decorated the CNTs uniformly, adopting a "beaded necklace-style" nanostructured morphology without forming a continuous layer. This nanostructuring was also retained when clusters were deposited under the same conditions on a Si wafer (Figure 1c), producing a 200 nm-thick layer with a granular morphology. This reference sample was deposited simultaneously with the NS-WO$_x$/CNT hybrid, ensuring the homogeneity of cluster production on both substrates.[39] The last sample investigated was fabricated by depositing a 25 nm WO$_x$ layer via DCMS on a CNT carpet similar to that used for the NS-WO$_x$/CNT hybrids. Its morphology, as shown in Figure 1d, revealed that the oxide layer coated the CNTs uniformly while preserving their morphology at the micrometer scale.

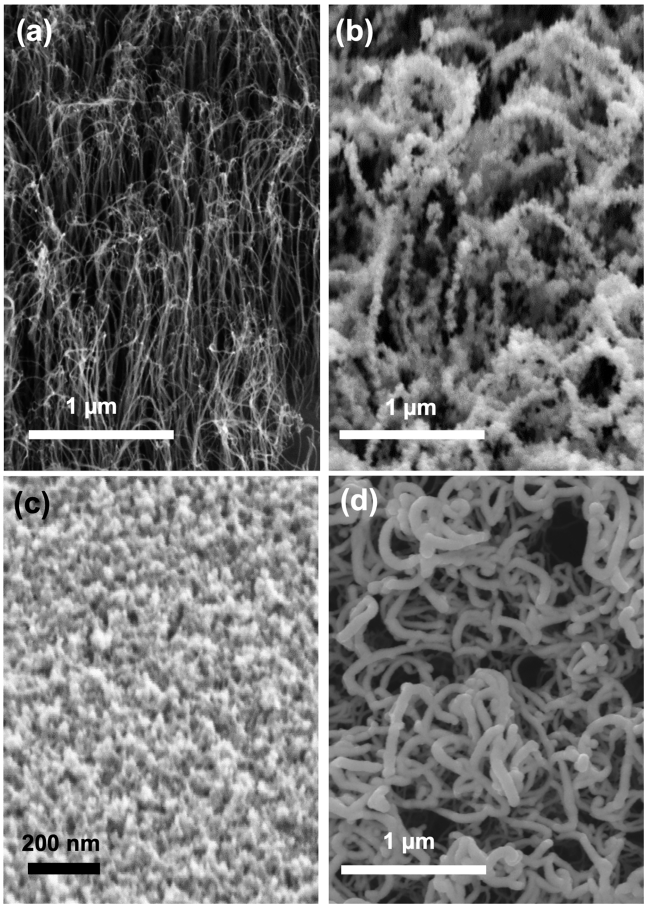


**Figure 1.** SEM images acquired on the various samples. (a) CNTs forest; (b) NS-WO$_x$/CNT hybrid deposited by the supersonic cluster beam source; (c) 200 nm NS-WO$_x$ layer on a Si wafer capped with native oxide; and (d) 25 nm WO$_x$ layer deposited on a CNT forest by magnetron sputtering.

It is important to remark that, to ensure homogeneous cluster coverage along the vertical height of the CNT carpet, we have selected CNT forests with a well-defined length and relatively low surface density, as specified earlier. This parameter proved crucial: excessively dense forests hinder the penetration of the cluster beam, leading to shadowing effects and incomplete decoration of the inner CNT walls. The chosen density guaranteed that the supersonic cluster beam could access the entire CNT length. As a control experiment, we deposited a 500 nm WO$_x$ film by DCMS onto a much denser CNT forest ($7.5 \times 10^3$ CNTs/$\mu$m$^2$). In this case (Figure S2, Supporting Information), a continuous microstructured oxide layer formed, while the vertical alignment of the CNTs was retained. This comparison highlights the crucial role of CNT density in determining the coating morphology. Based on these observations, we selected the CNT forest density that ensured a uniform nanocluster decoration along the entire nanotube length.

TEM investigations of the NS-WO$_x$ material were carried out to determine the crystalline structure of the clusters obtained via SCBD, and the results are shown in Figure 2.

The TEM images revealed the presence of nanoclusters exhibiting both amorphous and crystalline phases. Selected-area electron diffraction (SAED) patterns (left-hand panel of



https://doi.org/10.1021/acsaelm.5c01933
ACS Appl. Electron. Mater. 2025, 7, 10438−10445

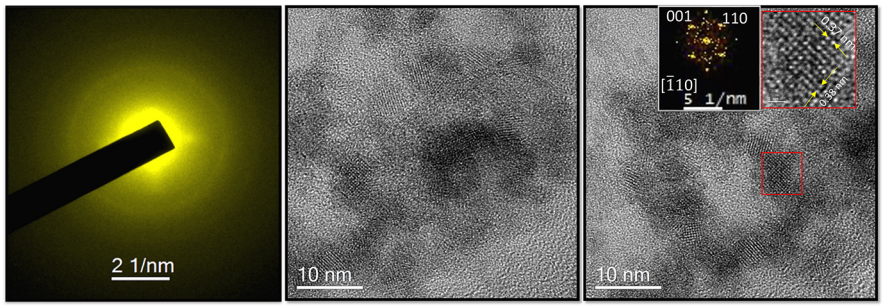


**Figure 2.** TEM characterization of the nanoparticle aggregates forming the NS-$WO_x$ layer on a Si wafer. The left panel shows the selected-area electron diffraction (SAED) pattern acquired from the sample, indicating partial crystallinity. The central and right panels show TEM micrographs from different regions of the sample. The inset in the right panel presents a magnified view of the area highlighted in red, along with the corresponding fast Fourier transform (FFT) pattern.

Figure 2) indicated rotational disorder but remained consistent with crystalline nanoparticles showing lattice spacings of 0.38 and 0.37 nm. These values correspond to the (001) and (110) planes of monoclinic $WO_3$, as highlighted in the right panel of Figure 2.

Further insights into the chemical environment and interfacial interactions within the hybrid systems were obtained through X-ray photoelectron spectroscopy (XPS). A comparative analysis of the W 4f and O 1s core levels was performed on four representative samples: NS-$WO_x$-CNT, NS-$WO_x$ on a Si wafer with native oxide, a 25 nm $WO_x$ film on CNTs, and a 200 nm $WO_x$ film on a Si wafer with native oxide.

Figure 3a shows the W 4f core-level spectra. In all cases, the W 4f spectra displayed the characteristic spin−orbit doublet,

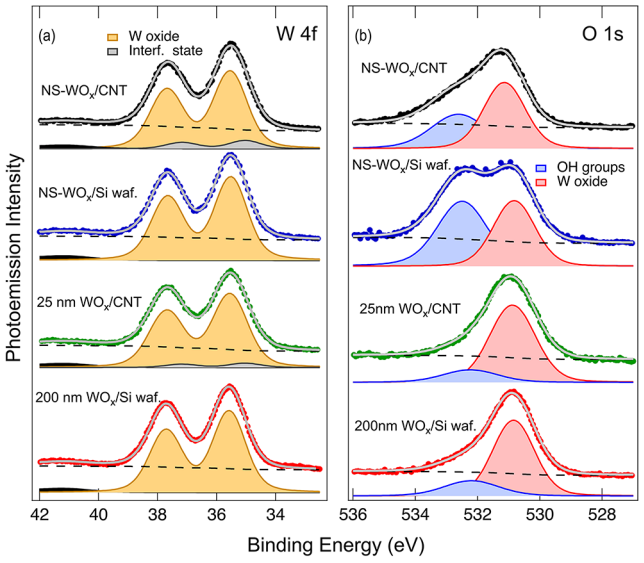


**Figure 3.** (a) W 4f and (b) O 1s spectra acquired on the different samples, as indicated in each panel. The filled colored dots represent the experimental data; the continuous gray line shows the best fit to the data using the spectral components (filled line profiles) and the background (dashed line) reported in each spectrum.

with the W $4f_{7/2}$ component centered at a binding energy (BE) of 35.5 eV, consistent with tungsten in the $W^{6+}$ oxidation state.[23,40] However, a distinct shoulder at lower binding energy (BE = 35.0 eV) appeared exclusively in the NS-$WO_x$-CNT and $WO_x$-CNT samples prepared by DCMS. In contrast, this feature was absent in the planar 200 nm $WO_x$/Si wafer sample, where the $WO_x$-substrate interface lays beyond the probing depth of the measurement. We interpreted this shoulder as an electronic signature of interfacial state formation, a feature already observed for $WO_3$-CNT systems.[26] Its selective appearance in the CNT-containing architectures suggested a chemically and electronically active interface that was absent in the systems containing only $WO_x$. Although the spectra were broad, the data obtained for the NS-$WO_x$-CNT hybrid and the $WO_x$-CNT samples could not be satisfactorily fitted using a single component with the same line shape adopted for the $WO_x$ film on the Si wafer.

More details about the chemical composition of the samples were obtained by analyzing the O 1s core level, shown in Figure 3b. The O 1s spectra displayed two main components: one at BE = 530.8 eV, attributed to oxygen in $WO_x$, and another at 532.5 eV, associated with surface hydroxyl groups formed upon air exposure. In the Si-wafer-supported samples, signals from the native $SiO_2$ layer were not detectable due to the limited probing depth of the technique. Overall, the XPS data confirmed the comparable average stoichiometry of the $WO_x$ phases obtained by different methods, while simultaneously revealing the formation of interface-specific electronic states exclusively in the CNT-based samples.

**Resistive Response to Ethanol.** The resistive response to ethanol for the various samples is reported in Figure 4. Specifically, we plot the sensitivity ($S$), as defined in the Experimental Section, as a function of ethanol exposure time. In the following, we adopt the terminology of p-type and n-type conductivity to describe the observed changes in sensitivity upon ethanol exposure. These terms refer to the dominant charge carriers in the material, i.e., holes in p-type and electrons in n-type systems, and to how their concentration is modulated by interaction with gas molecules. Ethanol, being a reducing gas, typically donates electrons to the system. In a simplified picture, in p-type materials this electron donation decreases the hole concentration, leading to an increase in electrical resistance; conversely, in n-type materials, ethanol increases the electron concentration, resulting in a decrease in resistance. This framework is widely used to interpret the gas-sensing behavior of metal oxides, carbon nanostructures, and their hybrid systems when exposed to reducing or oxidizing species.[41,42]

We first discuss the behavior of the individual components, followed by that of the hybrids. For the pristine CNT forest, the resistance increased gradually during EtOH exposure—a feature typical of p-type semiconductors interacting with reducing gases[9]—and recovered once the flux was stopped.


https://doi.org/10.1021/acsaelm.5c01933
ACS Appl. Electron. Mater. 2025, 7, 10438−10445

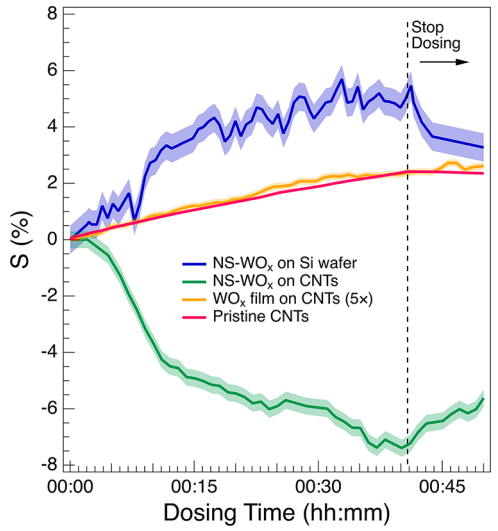


**Figure 4.** Sensitivity measurements of the various materials upon exposure to EtOH in UHV (partial pressure $p = 2 \times 10^{-5}$ mbar). The dashed line on the right indicates when EtOH exposure was stopped. The data for the $WO_x$ film grown by DCMS on CNTs (yellow) were multiplied by 5 to show that they follow the same trend as the pristine CNT sample but with reduced intensity. Shaded regions represent the corresponding error margins.

The maximum sensitivity observed in this work ($S$ = 2.42 ± 0.05%), measured in UHV, was significantly higher than values reported under atmospheric conditions, where humidity reduces CNT sensitivity.[43] The reproducibility of the measurement was verified (Figure S3, Supporting Information): repeating the experiment after a 24-h recovery period yielded identical response behavior. Furthermore, longer exposures (i.e., higher EtOH dose) led to higher final $S$ values (5.5 ± 0.05%), indicating that the response remained well below saturation.

In contrast, the $WO_x$ film grown on a Si wafer via DCMS showed only a modest and delayed resistance decrease of less than 1% (not shown), likely due to contact instabilities or limited adsorption sites. The $WO_x$ film grown via DCMS on CNTs under the same conditions exhibited a much lower sensitivity (0.47 ± 0.03%), following a response curve similar to that of the CNTs but with attenuated amplitude (approximately five times smaller). This behavior likely resulted from passivation of the CNT surface by the continuous oxide coating, which suppressed the p-type conduction typical of CNTs.

The nanostructured $WO_x$ (NS-$WO_x$) films, however, exhibited markedly different behavior. A significantly enhanced response was observed for the NS-$WO_x$ film grown via SCBD on Si wafers: at a total dose of $4.8 \times 10^4$ L EtOH (after 40 min), the sensitivity reached approximately 5.4 ± 0.5%, outperforming the CNTs. The response rapidly recovered once EtOH exposure ceased. Although stoichiometric $WO_3$ behaves as an n-type semiconductor at high temperatures,[26,44] substoichiometric tungsten oxides can exhibit p-type conduction at room temperature.[45] This behavior matched that of our NS-$WO_x$/Si wafer sample and can be attributed to structural defects, visible in SEM and TEM, that accept electrons and enable hole conduction. It has been reported that sufficiently reduced $WO_{3-x}$ achieves effective p-type behavior, supporting charge transport mechanisms distinct from those of stoichiometric $WO_3$.[44] Vacuum annealing these samples at 550 K for 10 min did not alter the XPS line shapes but reduced the sensitivity $S$ from 5.5 to 1.4% (Figure S4), suggesting that oxygen defects govern the interaction with the reducing gas and that structural reordering upon annealing hinders this process.

The most striking behavior was observed for the NS-$WO_x$-CNT hybrids. These displayed a negative resistance response, reaching a sensitivity of −7.3 ± 0.3% at the same EtOH dose as the other materials, with rapid onset and recovery. Such an inverted trend, consistent with n-type conduction, is rarely observed in CNT-based systems. We propose that this atypical behavior arises from interfacial electron transfer between the highly defective tungsten oxide nanoclusters and the underlying CNTs. This interpretation is supported by the contrasting behavior of the DCMS-grown $WO_x$-CNT film, where a compact oxide layer suppresses such interactions, effectively passivating the CNT surface and hindering charge exchange.

A second series of sensitivity tests assessed pressure-dependent responses, relevant for sensing applications (Figure S5). These revealed an even higher sensitivity ($S$ = − 14.0 ± 0.3%) when the NS-$WO_x$-CNT hybrids were exposed to higher ethanol pressure ($3 \times 10^{-4}$ mbar). It is worth nothing that the initial phase of this second exposure was performed at the same pressure as the first set (Figure 4) and yielded a comparable response, confirming the persistence of the electronic structure modification at the hybrid interface. Remarkably, the sensitivity of our hybrids remained stable even after prolonged air exposure. The samples were synthesized, exposed to air for SEM and TEM characterization, and later reintroduced into UHV for resistivity measurements, maintaining performance after several weeks under ambient conditions. These characteristics underscore the potential of NS-$WO_x$-CNT hybrids as reliable, air-stable n-type materials for CNT-based sensing and electronic devices.

A stable n-type conduction response in CNT-based hybrids at room temperature is both technologically valuable and fundamentally rare. While the measured resistance change represents the collective response of the hybrid film, the inverted sign indicates dominant n-type behavior induced by interfacial charge transfer. Most n-doping routes for CNTs lack stability under ambient conditions.[32] Previous reports have shown that hybridization with transition-metal oxides can modulate the electronic properties of CNTs, notably by shifting their Fermi level and inducing n-type behavior, both for Mo[46] and W oxides.[26,47] As previously noted, oxygen-deficient $WO_{3-x}$ structures act as electron donors that transfer charge to adjacent CNTs through oxygen vacancies,[17,23,44,45] effectively raising the CNT Fermi level and modifying their electronic structure. Experimental reports corroborate this mechanism,[15,23,41,45,47] showing that oxygen vacancies in $WO_3$ enhance both electrical conductivity and carrier density, thereby strengthening interfacial charge transfer. Our findings are consistent with this picture, indicating that interfacial charge transfer from oxygen-deficient nanostructured $WO_x$ to CNTs induces robust n-type behavior.

Overall, $WO_x$ nanoclusters introduce donor-like electronic states at the interface, creating favorable conditions for stable n-type conduction in our hybrids under the explored environmental conditions. Conversely, this behavior is absent in continuous oxide films, as observed for our DCMS $WO_3$/CNT sample, underscoring the importance of a defective,


https://doi.org/10.1021/acsaelm.5c01933
ACS Appl. Electron. Mater. 2025, 7, 10438−10445

nanostructured oxide phase in activating these interfacial electronic features.

## CONCLUSIONS

In this work, we demonstrated a link between morphology, interfacial chemistry, and charge transport in $WO_x$/CNT hybrid nanostructures. By means of supersonic cluster beam deposition, we obtained a distinctive "beaded-necklace" arrangement of oxygen-deficient $WO_x$ nanoclusters on vertically aligned CNTs, which induced upon ethanol response a reproducible inversion from the typical p-type response of CNTs to a stable behavior compatible with n-type conduction. The observed negative resistance variation, together with the interface-specific states revealed by XPS, highlighted the crucial role of oxygen vacancies and interfacial charge transfer in governing the electronic structure of the hybrids. Unlike conventional n-doping strategies for CNTs, which often lack ambient stability, the present approach achieved persistent n-type conduction even after prolonged air exposure. Our results, interpreted within the broader context of oxide/CNT hybrid literature, point to a general mechanism whereby oxygen-vacancy-rich oxide nanostructures establish donor-like interfacial states that inject electrons into the carbon network, shifting its Fermi level and inverting the conduction type. These findings contribute to the understanding of oxide−CNT interactions and provide a practical route for designing CNT-based platforms with controlled conduction type, offering a promising pathway toward robust, room-temperature sensors and emerging nanoelectronic architectures.

## ASSOCIATED CONTENT

### Data Availability Statement

The authors have provided the data in the main manuscript and in the Supporting Information file. Any further data is available from the corresponding author upon reasonable request.

### Supporting Information

The Supporting Information is available free of charge at https://pubs.acs.org/doi/10.1021/acsaelm.5c01933.

Geometry of the contacts during resistive response measurements (Figure S1); SEM image of the FIB cross section of the 500 nm $WO_x$ layer deposited by DCMS on the CNT forest (Figure S2); exposure of a CNT-forest sample to EtOH in UHV ($p = 2 \times 10^{-5}$ mbar), to verify the reproducibility of the response and find the saturation dose (Figure S3); sensitivity response of the NS-$WO_x$ deposited on the Si wafer during exposure to EtOH in UHV before and after thermal annealing (Figure S4); and exposure to EtOH of the NS-$WO_x$/CNT hybrid in two different pressure regimes (Figure S5) (PDF)

## AUTHOR INFORMATION


### Corresponding Authors

**Luca Bignardi** − *Department of Physics, University of Trieste, 34127 Trieste, Italy; CNR - Istituto Officina dei Materiali (IOM), AREA Science Park, 34149 Trieste, Italy;* orcid.org/0000-0002-9846-9100; Email: lbignardi@units.it

**Cinzia Cepek** − *CNR - Istituto Officina dei Materiali (IOM), AREA Science Park, 34149 Trieste, Italy*; Email: cepek@iom.cnr.it

### Authors

**Ayesha Farooq** − *CNR - Istituto Officina dei Materiali (IOM), AREA Science Park, 34149 Trieste, Italy; Department of Physics, University of Trieste, 34127 Trieste, Italy;* Present Address: Department of Physics, COMSATS University Islamabad, Park Road, Tarlai Kalan, Islamabad 45550, Pakistan

**Matus Stredansky** − *CNR - Istituto Officina dei Materiali (IOM), AREA Science Park, 34149 Trieste, Italy;* Present Address: School of Chemistry, The University of Birmingham, Edgbaston, Birmingham B15 2TT, U.K.

**Marco Caputo** − *Elettra Sincrotrone Trieste, AREA Science Park, 34149 Trieste, Italy*

**Sharath Sasikumar** − *European XFEL, 22869 Schenefeld, Germany;* Present Address: Dipartimento di Fisica "Aldo Pontremoli", Università degli Studi di Milano, via Celoria 16, 20133 Milano, Italy.

**Ferdinando Bassato** − *CNR - Istituto Officina dei Materiali (IOM), AREA Science Park, 34149 Trieste, Italy;* orcid.org/0000-0002-2775-2662

**Regina Ciancio** − *AREA Science Park, 34149 Trieste, Italy*

**Simone Dal Zilio** − *CNR - Istituto Officina dei Materiali (IOM), AREA Science Park, 34149 Trieste, Italy;* orcid.org/0000-0003-0337-7068

**Andrea Goldoni** − *Elettra Sincrotrone Trieste, AREA Science Park, 34149 Trieste, Italy*

**Paolo Piseri** − *Dipartimento di Fisica "Aldo Pontremoli", Università degli Studi di Milano, 20133 Milano, Italy*

**Tommaso Mazza** − *European XFEL, 22869 Schenefeld, Germany;* orcid.org/0000-0003-3105-459X

**Silvia Rubini** − *CNR - Istituto Officina dei Materiali (IOM), AREA Science Park, 34149 Trieste, Italy;* orcid.org/0000-0001-5215-2223

Complete contact information is available at: https://pubs.acs.org/10.1021/acsaelm.5c01933


### Author Contributions

A.F. and L.B. contributed equally to this work. C.C.: Conceptualization; All authors: Methodology; A.F., C.C., and L.B.: Formal analysis; All Authors: Investigation; C.C.: Funding Aquisition; C.C.: Supervision; C.C., L.B., and S.R.: Writing—original draft; All authors: Writing—review and editing.

### Notes

The authors declare no competing financial interest.

## ACKNOWLEDGMENTS

C.C. and F.B. acknowledge the European Union NextGeneration EU, Piano Nazionale di Ripresa e Resilienza (PNRR), Missione 4 Componente 2, Investimento 1.3, Fondazione NEST, "Network 4 Energy Sustainable Transition", Spoke 4, Clean hydrogen and Final uses (grant no. PE00000021). L.B. acknowledges support from the Microgrants support program of the University of Trieste. C.C., P.P, T.M., and S.S. acknowledge funding from the European Union's Horizon 2020 Research and Innovation Programme under grant agreement No. 654360, having benefitted from the access provided by CNR-IOM in Trieste (Italy), within the framework of the NFFA-Europe Transnational and European Union's Horizon 2020 Research and Innovation Program under grant agreement No. 101007417, NFFA-Europe Pilot. C.C. and A.F. acknowledge JRA Eni-CNR Linea 3.

## REFERENCES


(1) Gomez-Romero, P.; Pokhriyal, A.; Rueda-Garcia, D.; Bengoa, L. N.; González-Gil, R. M. Hybrid materials: A metareview. *Chem. Mater.* **2024**, *36*, 8−27.

(2) Garcia-Martinez, J. M.; Collar, E. P. Current and future insights in organic–inorganic hybrid materials. *Polymers* **2024**, *16*, 3043.

(3) Hughes, K. J.; Iyer, K. A.; Bird, R. E.; Ivanov, J.; Banerjee, S.; Georges, G.; Zhou, Q. A. Review of carbon nanotube research and development: Materials and emerging applications. *ACS Appl. Nano Mater.* **2024**, *7*, 18695−18723.

(4) Wang, K.; Wang, F.; Jiang, Q.; Zhu, P.; Leu, K.; Zhang, R. Controlled synthesis, properties, and applications of ultralong carbon nanotubes. *Nanoscale Adv.* **2024**, *6*, 4504−4521.

(5) Dubey, R.; Dutta, D.; Sarkar, A.; Chattopadhyay, P. Functionalized carbon nanotubes: Synthesis, properties and applications in water purification, drug delivery, and material and biomedical sciences. *Nanoscale Adv.* **2021**, *3*, 5722−5744.

(6) Avouris, P.; Radosavljević, M.; Wind, S. In *Applied Physics of Carbon Nanotubes*, Rotkin, S. V., Subramoney, S., Eds.; Springer: Berlin, 2005; pp 159−194.

(7) Schroeder, V.; Savagatrup, S.; He, M.; Lin, S.; Swager, T. M. Carbon nanotube chemical sensors. *Chem. Rev.* **2019**, *119*, 599−663.

(8) Han, T.; Nag, A.; Chandra Mukhopadhyay, S.; Xu, Y. Carbon nanotubes and its gas-sensing applications: A review. *Sens. Actuators, A* **2019**, *291*, 107−143.

(9) Wongchoosuk, C.; Wisitsoraat, A.; Phokharatkul, D.; Tuantranont, A.; Kerdcharoen, T. Carbon Nanotube Composites for Formaldehyde Detection. *Sensors* **2010**, *10*, 7705−7715.

(10) Raya, I.; Kzar, H. H.; Mahmoud, Z. H.; Al Ayub Ahmed, A.; Ibatova, A. Z.; Kianfar, E. A review of gas sensors based on carbon nanomaterials. *Carbon Lett.* **2022**, *32*, 339−357.

(11) Hejazi, M. A.; Eksik, O.; Taşdelen-Yücedağ, Ç.; Ünlü, C.; Trabzon, L. Carbon-based nanomaterials in gas sensing applications. *Emergent Mater.* **2023**, *6*, 45−59.

(12) Long, H.; Zeng, W.; Zhang, H. Synthesis of $WO_3$ and its gas sensing: A review. *J. Mater. Sci.: Mater. Electron.* **2015**, *26*, 4698−4707.

(13) Li, H.; Shen, Q.; Zhang, H.; Gao, J.; Jia, H.; Liu, X.; Li, Q.; Xue, J. Oxygen vacancy-mediated $WO_3$ phase junction to steering photogenerated charge separation for enhanced water splitting. *J. Adv. Ceram.* **2022**, *11*, 1873−1888.

(14) An, F.; Zhou, A. F.; Feng, P. X. Effect of tungsten oxide nanostructures on sensitivity and selectivity of pollution gases. *Sensors* **2020**, *20*, 4801.

(15) Zheng, H.; Ou, J. Z.; Strano, M. S.; Kaner, R. B.; Mitchell, A.; Kalantar-zadeh, K. Nanostructured tungsten oxide—Properties, synthesis, and applications. *Adv. Funct. Mater.* **2011**, *21*, 2175−2196.

(16) Li, X.; Fu, L.; Karimi-Maleh, H.; Chen, F.; Zhao, S. Innovations in $WO_3$ gas sensors: Nanostructure engineering, functionalization, and future perspectives. *Heliyon* **2024**, *10*, No. e27740.

(17) Wang, Y.; Li, J.; Xiao, D.; Zhang, D.; Liu, Y.; Sun, M.; Chen, S.; Sun, M. Progress in functionalized $WO_3$-based gas sensors for selective $H_2S$ and $NH_3$: A review. *Ceram. Int.* **2024**, *50*, 40631−40665.

(18) Lin, T.; Lv, X.; Li, S.; Wang, Q. The morphologies of the semiconductor oxides and their gas-sensing properties. *Sensors* **2017**, *17*, 2779.

(19) Mirzaei, A.; Leonardi, S. G.; Neri, G. Detection of hazardous volatile organic compounds (VOCs) by metal oxide nanostructures-based gas sensors: A review. *Ceram. Int.* **2016**, *42*, 15119−15141.

(20) Abdulkadir, B.; Setiabudi, H. Recent advances in multi-walled carbon nanotubes for high-efficient solid-state hydrogen storage: a review. *Chem. Eng. Technol.* **2025**, *48*, No. e202400067.

(21) Greiner, M.; Chai, L.; Helander, M. G.; Tang, W. M.; Lu, Z. Transition metal oxide work functions: the influence of cation oxidation state and oxygen vacancies. *Adv. Funct. Mater.* **2012**, *22*, 4557−4568.

(22) Tokura, Y.; Nagaosa, N. Orbital physics in transition-metal oxides. *Science* **2000**, *288*, 462−468.

(23) Chen, P.; Baldwin, M.; Bandaru, P. R. Hierarchically structured, oxygen deficient, tungsten oxide morphologies for enhanced photoelectrochemical charge transfer and stability. *J. Mater. Chem. A* **2017**, *5*, 14898−14905.

(24) Yao, Y.; Yin, M.; Yan, J.; Liu, S. F. P-type sub-tungsten-oxide based urchin-like nanostructure for superior room temperature alcohol sensor. *Appl. Surf. Sci.* **2018**, *441*, 277−284.

(25) Eder, D. Carbon nanotube–inorganic hybrids. *Chem. Rev.* **2010**, *110*, 1348−1385.

(26) Bittencourt, C.; Felten, A.; Espinosa, E. H.; Ionescu, R.; Llobet, E.; Correig, X.; Pireaux, J. J. $WO_3$ films modified with functionalised multi-wall carbon nanotubes: Morphological, compositional and gas response studies. *Sens. Actuators, B* **2006**, *115*, 33−41.

(27) Wang, T.; Hao, J.; Zheng, S.; Sun, Q.; Zhang, D.; Wang, Y. Highly sensitive and rapidly responding room-temperature $NO_2$ gas sensors based on $WO_3$ nanorods/sulfonated graphene nanocomposites. *Nano Res.* **2018**, *11*, 791−803.

(28) Shankar, N.; Yu, M.-F.; Vanka, S. P.; Glumac, N. G. Synthesis of tungsten oxide ($WO_3$) nanorods using carbon nanotubes as templates by hot filament chemical vapor deposition. *Mater. Lett.* **2006**, *60*, 771−774.

(29) Farhadian, M.; Sangpour, P.; Hosseinzadeh, G. Preparation and photocatalytic activity of $WO_3$–MWCNT nanocomposite for degradation of naphthalene under visible light irradiation. *RSC Adv.* **2016**, *6*, 39063−39073.

(30) Tian, L.; Ye, L.; Liu, J.; Zan, L. Solvothermal synthesis of CNTs–$WO_3$ hybrid nanostructures with high photocatalytic activity under visible light. *Catal. Commun.* **2012**, *17*, 99−103.

(31) Duong, V. T.; Nguyen, C. T.; Luong, H. B.; Nguyen, D. C.; Nguyen, H. L. Ultralow-detection limit ammonia gas sensors at room temperature based on MWCNT/$WO_3$ nanocomposite and effect of humidity. *Solid State Sci.* **2021**, *113*, No. 106534.

(32) Brownlie, L.; Shapter, J. Advances in carbon nanotube n-type doping: Methods, analysis and applications. *Carbon* **2018**, *126*, 257−270.

(33) Ramirez de Arellano, J. M.; Canales, M.; Magaña, L. F. Carbon nanostructures doped with transition metals for pollutant gas adsorption systems. *Molecules* **2021**, *26*, 5346.

(34) Navrotskaya, A. G.; Aleksandrova, D. D.; Krivoshapkina, E. F.; Sillanpää, M.; Krivoshapkin, P. V. Hybrid materials based on carbon nanotubes and nanofibers for environmental applications. *Front. Chem.* **2020**, *8*, 546.

(35) Lee, J. A.; Lee, J. Y.; Lim, J.; Kim, S. O. N-dopant-mediated growth of metal oxide nanoparticles on carbon nanotubes. *Nanomaterials* **2021**, *11*, 1882.

(36) Wegner, K.; Piseri, P.; Tafreshi, H. V.; Milani, P. Cluster beam deposition: A tool for nanoscale science and technology. *J. Phys. D: Appl. Phys.* **2006**, *39*, R439−R459.

(37) Baer, D. R.; Lea, A. S.; Sindelar, R. L. Practical guides for X-ray photoelectron spectroscopy: First steps in planning, conducting, and reporting XPS measurements. *J. Vac. Sci. Technol., A* **2019**, *37*, No. 031401.

(38) Mbuyisa, P. N.; Rigoni, F.; Nappini, S.; Magnano, E.; Pagliara, S.; Drera, G.; Sangaletti, L.; Goldoni, A.; Ndwandwe, M.; Cepek, C. Fast-tracking of $NH_3$ interaction with ZnO nanorods and C/ZnO hybrid nanostructures by operando spectroscopy. *Appl. Surf. Sci.* **2022**, *590*, No. 153067.

(39) Hwang, N. M. *Non-Classical Crystallization of Thin Films and Nanostructures in CVD and PVD Processes*; Springer: Dordrecht, 2016.

(40) Mazur, M.; Wojcieszak, D.; Wiatrowski, A.; Kaczmarek, D.; Lubańska, A.; Domaradzki, J.; Mazur, P.; Kalisz, M. Analysis of amorphous tungsten oxide thin films deposited by magnetron sputtering for application in transparent electronics. *Appl. Surf. Sci.* **2021**, *570*, No. 151151.

(41) Ji, H.; Zeng, W.; Li, Y. Gas sensing mechanisms of metal oxide semiconductors: A focus review. *Nanoscale* **2019**, *11*, 22664−22684.

(42) Wang, C.; Yin, L.; Zhang, L.; Xiang, D.; Gao, R. Metal oxide gas sensors: Sensitivity and influencing factors. *Sensors* **2010**, *10*, 2088−2106.




https://doi.org/10.1021/acsaelm.5c01933
*ACS Appl. Electron. Mater.* 2025, 7, 10438−10445

(43) Young, S.-J.; Lin, Z.-D. Ethanol gas sensors based on multi-wall carbon nanotubes on oxidized Si substrate. *Microsyst. Technol.* **2018**, *24*, 55−58.
(44) Modak, M.; Rane, S.; Jagtap, S. $WO_3$: A review of synthesis techniques, nanocomposite materials and their morphological effects for gas sensing application. *Bull. Mater. Sci.* **2023**, *46*, 28.
(45) Al Hashem, M.; Akbar, S.; Morris, P. Role of oxygen vacancies in nanostructured metal-oxide gas sensors: A review. *Sens. Actuators, B* **2019**, *301*, No. 126845.
(46) Men, Y.-L.; Dou, N.; Zhao, Y.; Huang, Y.; Zhang, L.; Liu, P. Boosted Electrocatalytic Glucose Oxidation Reaction on Noble-Metal-Free $MoO_3$-Decorated Carbon Nanotubes *Trans. Tianjin Univ.* **2024**, *30*, 63−73.
(47) Huang, Z.; Li, H.; Li, W.; Henkelman, G.; Jia, B.; Ma, T. Electrical and structural dual function of oxygen vacancies for promoting electrochemical capacitance in tungsten oxide. *Small* **2020**, *16*, No. 2004709.





https://doi.org/10.1021/acsaelm.5c01933
*ACS Appl. Electron. Mater.* 2025, 7, 10438−10445